

# Kinematic fields measurement during Ti-6Al-4V chip formation using new high-speed imaging system

Haythem Zouabi (✉ [haythem.zouabi@u-bordeaux.fr](mailto:haythem.zouabi@u-bordeaux.fr))

University of Bordeaux: Universite de Bordeaux

**Madalina Calamaz**

University of Bordeaux

**Vincent Wagner**

Université de Toulouse

**Olivier Cahuc**

Univeristy of Bordeaux

**Gilles Dessein**

Université de Toulouse

---

## Research Article

**Keywords:** Chip formation, High-speed optical system, In-situ measurement, Digital Image Correlation, kinematic fields

**Posted Date:** April 5th, 2022

**DOI:** <https://doi.org/10.21203/rs.3.rs-1435161/v1>

**License:**   This work is licensed under a Creative Commons Attribution 4.0 International License.

[Read Full License](#)

---

# Kinematic fields measurement during Ti-6Al-4V chip formation using new high-speed imaging system

Haythem Zouabi<sup>1\*</sup>, Madalina Calamaz<sup>2</sup>, Vincent  
Wagner<sup>3</sup>, Olivier Cahuc<sup>1</sup> and Gilles Dessein<sup>3</sup>

<sup>1\*</sup>Univeristy of Bordeaux, CNRS, Arts et Métiers Institute of  
Technology, Bordeaux INP, INRAE, I2M Bordeaux, F-33400  
Talence, France.

<sup>2</sup>Arts et Métiers Institute of Technology, University of Bordeaux,  
CNRS, Bordeaux INP, INRAE, HESAM Université, I2M  
Bordeaux, F-33400 Talence, France.

<sup>3</sup>Laboratoire Génie de Production, ENIT-INPT, Université de  
Toulouse, Tarbes 65440, France.

\*Corresponding author(s). E-mail(s):

[haythem.zouabi@u-bordeaux.fr](mailto:haythem.zouabi@u-bordeaux.fr);

Contributing authors: [madalina.calamaz@ensam.eu](mailto:madalina.calamaz@ensam.eu);

[vincent.wagner@enit.fr](mailto:vincent.wagner@enit.fr); [olivier.cahuc@u-bordeaux.fr](mailto:olivier.cahuc@u-bordeaux.fr);

[gilles.dessein@enit.fr](mailto:gilles.dessein@enit.fr);

## Abstract

In-situ visualization of the material flow during orthogonal cutting is achieved using new high-speed optical system. Difficulties arise from the submillimetric size of the cutting zone. Therefore, a dedicated optical system was designed allowing for local scale analysis of chip formation. The Digital Image Correlation (DIC) technique is applied on recorded images from the cutting zone to measure the kinematic fields. Then, the effect of the cutting conditions on chip formation is presented with local scale analysis.

**Keywords:** Chip formation; High-speed optical system; In-situ measurement; Digital Image Correlation; kinematic fields.

# 1 Introduction

Metal cutting is a widely used process for part manufacturing. During chip formation, the material is subjected to high strain ( $>1$ ) under high strain rate that can exceed  $10^3\text{s}^{-1}$ . Understanding the mechanisms of chip formation under complex thermomechanical loads require developing dedicated experimental set-up. In the cutting zone, the material undergoes high plastic deformation and local temperature rise that may induce changes in the material microstructure [1, 2] as well as its mechanical and physical properties. Establishing the link between the thermomechanical load and the material microstructure evolution leads to develop physical-based models [3–6] that are suitable for numerical simulation of the machining processes. Local measurement of the displacement and strain fields in the cutting zone are with a great importance to improve the machining process. These local fields measurement can be used to predict the stress fields within the cutting zone [7, 8].

In addition, local data measurements enables to enhance/validate numerical models that could better predict the thermomechanical load at local scale [9]. Numerical simulation results are mostly compared with the experimental ones at macroscopic level [10–13] through: i) force components measurement, ii) chip morphology and microstructure analysis and iii) temperature measurement at the tool tip [14–17]. These quantities remain global quantities and limit the understanding of local phenomena such as strain localization [18–20]. The highly interest in understanding local phenomena during chip formation has led researchers to develop a dedicated experimental protocol allowing for in-process visualization of the material flow in the cutting zone. Indeed, two major difficulties have to be mentioned: i) The submillimetric size of the region of interest (which disables any strain gauge to be mounted) and ii) the rapidity of the phenomenon (which disables to retrieve in real-time the kinematic fields).

First attempts to study the mechanisms of chip formation was made using Quik-Stop Devices (QSD) [21, 22]. It allows freezing the cutting process and extracting the chip root. Shear angle within the Primary Shear Zone (PSZ) could be measured. Despite the time delay for the tool-chip separation that induces errors, this technique gave results at only one instant which limits its use. An alternative technique allowing for in-situ visualization of chip formation was the use of high-speed camera. Particle tracking was achieved by printing a micro-scale grid [19, 20]. High distortion of the micro-scale grid induced by the high plastic deformation within the PSZ disables a full-field displacement measurement [20].

Recently, optical imaging systems have been successfully implemented for in-situ measurement of kinematic fields during machining [23–27]. They offer a real-time insight on the material flow through surface observation of the workpiece. Application of the DIC technique in the context of kinematic fields measurement during orthogonal cutting have been increased these last years[28]. It allows to measure a full-field displacement with sub-pixel

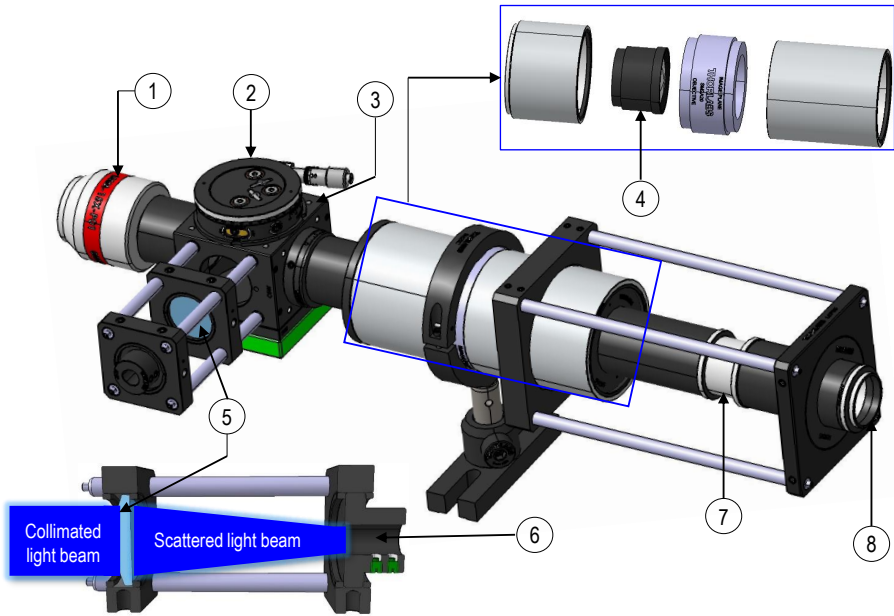
accuracy and to estimate the full-field strain. However, optical systems are constrained by the rapidity of physical phenomena and the out-of-plane motion of the chip ( $\pm 35\mu\text{m}$  as measured by Pottier et al during Ti-6Al-4V chip formation under a cutting speed of 6m/min). In fact, for local scale investigation, increasing the magnification of the lens leads for low depth of field. To overcome this issue, Baizeau et al [7] proposed the use of a telecentric X10 finite conjugate objective. The magnification value was enough for strain field measurement within the subsurface of the workpiece. On the other hand, Calamaz et al [29] employed a long distance microscope. The low spatial resolution of the microscope ( $3,34\mu\text{m}/\text{pixel}$ ) limits its use in the context of kinematic fields measurement within the cutting zone. Recently, Harzallah et al [25] proposed a new optical system ensuring a better spatial resolution. Besides, illuminating submillimetric zone remains one of the main problematics and authors didn't discuss about optical solutions.

In this paper, a dedicated optical system was designed for in-situ visualization of the material flow during orthogonal cutting. High-speed imaging of the cutting zone allows to follow the different phases of Ti-6Al-4V chip segmentation. The choice of the magnification objective is discussed. Then, a new optical solution is proposed for coaxial illumination that made possible to maximise the light intensity within submillimetric zone. In addition, it ensures uniformity in light distribution and allows to avoid under-exposure or over-exposure to light. The DIC technique was adopted for kinematic fields measurement. The application of the DIC technique is made on a sequence of images and not only 2 images. The choice of the DIC software was made so that it enables to determine the cumulative strain fields from the measured incremental ones. A Matlab script was developed for post-processing of the results returned by the DIC software. Orthogonal cutting tests were conducted on Ti-6Al-4V alloy. The experimental set-up is given. Results of the measured cutting forces are discussed. Application of the DIC technique allows to determine the kinematic fields that highlight localized shear band during Ti-6Al-4V chip formation.

## 2 Optical system

Under the camera resolution of  $512 \times 512 \text{ pixels}^2$ , an X15 magnification objective leads to obtain an acceptable scene size allowing for in-situ visualization of the material flow during chip formation. An infinity-corrected X15 magnification objective and coupled with a 200mm tube lens. The main reason behind choosing an infinity-corrected objective is that it enables introducing beam-splitter for coaxial illumination in the so-called infinity space delimited by the objective and the tube lens. Details of the optical system are given in figure 1.

The main characteristics of the optical system's components are given as follow:



1	X15 infinity corrected objective	5	F60mm plano-convex lens
2	Rotating platform	6	Fiber optic housing
3	30mm cube cage	7	SM1 coupler
4	200mm tube lens	8	C-mount adapter

**Fig. 1** New high-speed imaging system dedicated for kinematic fields measurement during orthogonal cutting

- the X15 infinity-corrected objective (1) ensures a transmittance up to 96% over the spectral band ranging between 450nm and 20000nm. This type of objective can be then used with a high-speed camera for visual imaging and also with an infrared camera for thermal inspection. The field of view of the objective is equal to  $1,2 \times 1,2 \text{mm}^2$ . The working distance of the objective is equal to 23,8mm.
- the rotating platform (2) is used to adjust a beam-splitter at  $45^\circ$  with respect to the optical axis. This beam-splitter ensures a 50% of reflectance and a 50% of transmittance in the spectral band ranging between 400 and 700nm. Both the rotating platform and the beam-splitter are mounted in a 30mm cube cage.
- Cold light source of 150W is used for illumination. The collimated light beam is obtained by mean of the f60mm plano-convex lens (5). It features an AntiReflective (AR) coating for the spectral band ranging between 350nm and 700nm. This new optical solution allows to maximize the light intensity while illuminating submillimetric zone.

- the tube lens (4) with a focal length equal to 200mm is used allowing to keep the magnification of the objective at X15. It ensures a transmittance up to 90% in the visible spectrum band. The distance that should separate the tube lens from the sensor array of the high-speed camera is equal to 148mm. For that, an SM1 coupler (7) is used for adjustment.
- the C-mount adapter (8) is used to connect the optical system with high-speed camera.

This optical system was designed specifically for high-speed imaging of the cutting zone. It allows to follow the different phases of Ti-6Al-4V chip segmentation. By application of the DIC technique on the recorded images, the kinematic fields are measured. Thus, the mechanisms of chip formation during orthogonal cutting on Ti-6Al-4V are analysed from the measured displacements and strains fields at local scale.

### 3 Digital Image Correlation

In this paper, the DIC technique was used for kinematic fields measurement during Ti-6Al-4V chip formation. Indeed, it ensures enough spatial resolution for localized shear band identification.

To evaluate the similarity between a given subset in the reference image and the corresponding one in the deformed image, a correlation criterion should be introduced. In this work, a Zero-Normalized Sum of Squared Differences (ZNSSD) correlation criterion was used:

$$C_{ZNSSD} = \sum_{i=-M}^M \sum_{j=-M}^M \left[ \frac{f(X_i, Y_j) - f_m}{\Delta f} - \frac{g(x_i, y_j) - g_m}{\Delta g} \right]^2 \quad (1)$$

where  $f(X_i, Y_j)$  is the gray level at pixel in the position  $(X_i, Y_j)$  in the reference image;  $g(x_i, y_j)$  is the gray level of the corresponding pixel in the deformed image;  $2M+1$  is the size of the subset centered at  $(X_0, Y_0)$  (respectively  $(x_0, y_0)$ ) in the reference image (respectively in the deformed image) and:

$$\begin{cases} f_m = \frac{1}{(2M+1)^2} \sum_{i=-M}^M \sum_{j=-M}^M f(X_i, Y_j) \\ g_m = \frac{1}{(2M+1)^2} \sum_{i=-M}^M \sum_{j=-M}^M g(x_i, y_j) \end{cases} \quad (2)$$

$$\begin{cases} \Delta f = \sqrt{\sum_{i=-M}^M \sum_{j=-M}^M [f(X_i, Y_j) - f_m]^2} \\ \Delta g = \sqrt{\sum_{i=-M}^M \sum_{j=-M}^M [g(x_i, y_j) - g_m]^2} \end{cases} \quad (3)$$

This correlation criterion ensures no sensitivity to both offset and linear scale in lighting [30] and indicates good match when  $C_{ZNSSD}$  is close to 0 (figure 2). In the reference image, the displacement components of each point  $(X_i, Y_j)$  are denoted by  $(U_{X_i}, U_{Y_j})$ .  $U_{X_i}$  (respectively  $U_{Y_j}$ ) is the displacement along the x-axis (respectively along y-axis). In the deformed image, the displacement components of each material points  $(x_i, y_j)$  are denoted by  $(U_{x_i}, U_{y_j})$ .

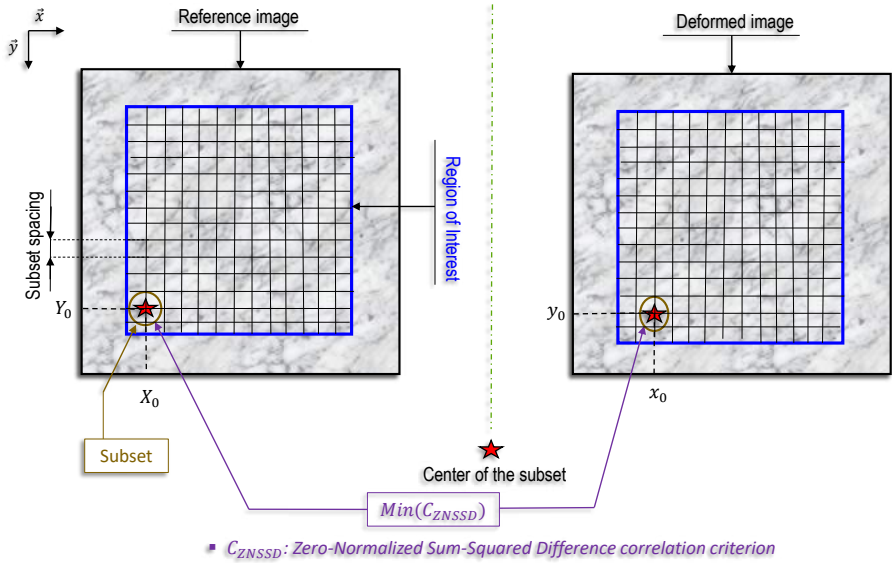


**Fig. 2** Illustration of the subset matching using the DIC technique with local approach.

### • Eulerian configuration

In this paper, Eulerian configuration was adopted so that the measured strain fields can be interpreted from the deformed images. In fact, when using eulerian configuration, the cumulative strain fields are given in the current (or the deformed image).

The components of the Eulerian-Almansi strain tensor computed from the displacement gradients are given by:

$$\begin{cases} A_{xx} = \frac{1}{2} [2 \frac{\partial U_x}{\partial x} - (\frac{\partial U_x}{\partial x})^2 - (\frac{\partial U_y}{\partial x})^2] \\ A_{xy} = \frac{1}{2} [\frac{\partial U_x}{\partial y} + \frac{\partial U_y}{\partial x} - \frac{\partial U_x}{\partial x} \frac{\partial U_x}{\partial y} + \frac{\partial U_y}{\partial x} \frac{\partial U_y}{\partial y}] \\ A_{yy} = \frac{1}{2} [2 \frac{\partial U_y}{\partial y} - (\frac{\partial U_x}{\partial y})^2 - (\frac{\partial U_y}{\partial y})^2] \end{cases} \quad (4)$$

Direct differentiation of the displacement field is sensitive to noise. This means that noise in the measured displacement field leads to errors in the strain field obtained by direct differentiation. In order to overcome this issue, Ncorr DIC software [31] uses a least squares plane fit on the displacement data within a strain calculation window of a given radius (figure 3) to determine the displacement gradients:

$$\begin{cases} U_{x,plane}(x, y) = a_{U_x,plane} + (\frac{\partial U_x}{\partial x})x + (\frac{\partial U_x}{\partial y})y \\ U_{y,plane}(x, y) = a_{U_y,plane} + (\frac{\partial U_y}{\partial x})x + (\frac{\partial U_y}{\partial y})y \end{cases} \quad (5)$$

where  $(U_{x,plane}, U_{y,plane})$  are the displacement components obtained by the least squares plane fit and  $(a_{U_x,plane}, a_{U_y,plane})$  are the parameters of the

fitting.

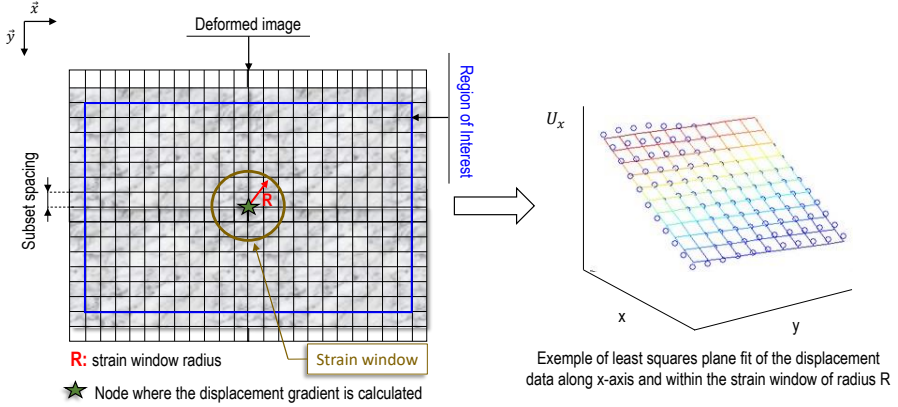


**Fig. 3** Illustration of the least squares plane fit on the displacement data to determine the displacement gradient.

Principal strains,  $A_M$  and  $A_m$  where  $A_M$  (respectively  $A_m$ ) denotes the major strain (respectively the minor strain) are defined as the eigenvalues of the strain tensor:

$$\begin{cases} A_M = \frac{A_{xx} + A_{yy}}{2} + \frac{1}{2} \sqrt{(A_{xx} - A_{yy})^2 + 4A_{xy}^2} \\ A_m = \frac{A_{xx} + A_{yy}}{2} - \frac{1}{2} \sqrt{(A_{xx} - A_{yy})^2 + 4A_{xy}^2} \end{cases} \quad (6)$$

The equivalent strain is then given by:

$$A_{eq} = \sqrt{\frac{2}{3}(A_M^2 + A_m^2)} \quad (7)$$

A Matlab script (figure 4) was developed to convert the displacement fields from pixel to micron unit. In addition, it is used to compute the minor, the major and the equivalent strain fields. Knowing the image size, this script allows to superimpose all the measured fields (displacement, strain and equivalent strain fields) on visual images captured by the high-speed camera.

In this paper, DIC technique is applied on the recorded images of one segment chip for kinematic fields measurement. The effect of the rake angle is examined through the results of the measured strain fields. Comparison between the equivalent strain reached within the localized shear band in the case using  $0^\circ$  and  $15^\circ$  rake angle is made.

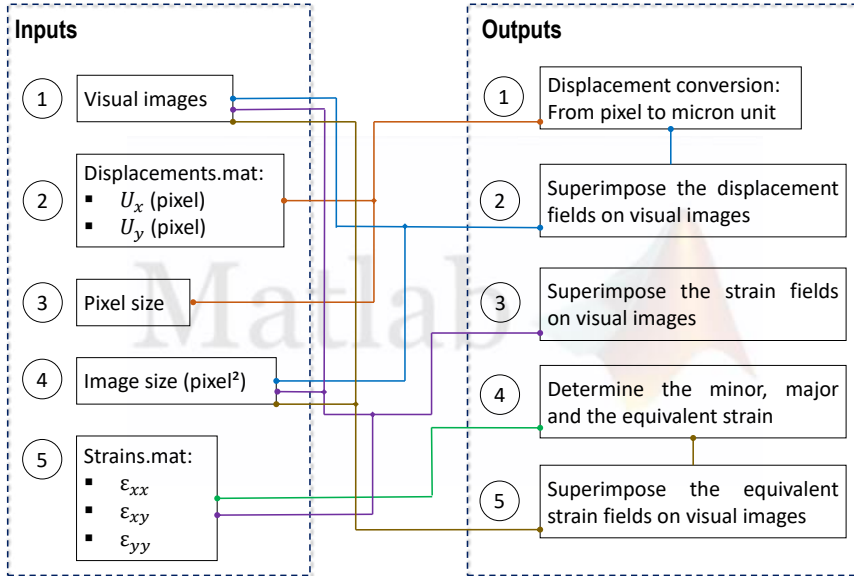


**Fig. 4** Description of the developed script: inputs, outputs and links.

## 4 Experimental set-up

Orthogonal cutting tests are made on rectangular Ti-6Al-4V workpiece under a cutting speed  $V_c=3\text{m/min}$  and a feed  $a=0,2\text{mm}$ . The width of cut is equal to 3mm. The workpiece surface side (figure 5) was polished and etched using a Kroll solution in order to reveal the material microstructure considered as a natural speckle for particle tracking.

Low cutting speed was chosen in order to validate the new high-speed optical system. Moreover, the adjustment of the optical parameters under 3m/min leads to obtain contrasted images that is suitable for DIC application as first-conducted test on Ti-6Al-4V alloy. H13A uncoated carbide cutting inserts were used. The experimental bench used for instrumented orthogonal cutting tests is given in figure 6. The first test was made with a rake angle of  $0^\circ$  while the second one was with  $15^\circ$  rake angle. The clearance angle in both tests was equal to  $11^\circ$ . Perpendicularity of the workpiece surface with respect to the tool rake face was adjusted to  $(0, +10\mu\text{m})$ . Figure 7 gives the experimental set-up used for high-speed imaging of the cutting zone.

### Cutting forces

Kistler 9129AA dynamometer was used for the cutting efforts measurements.  $F_c$  denotes the cutting force (along x-axis) and  $F_f$  is the feed force (along y-axis). The acquisition frequency was set to 20000Hz. Figure 8 gives the evolution of the cutting forces. The mean values as well as the maximum and the minimum

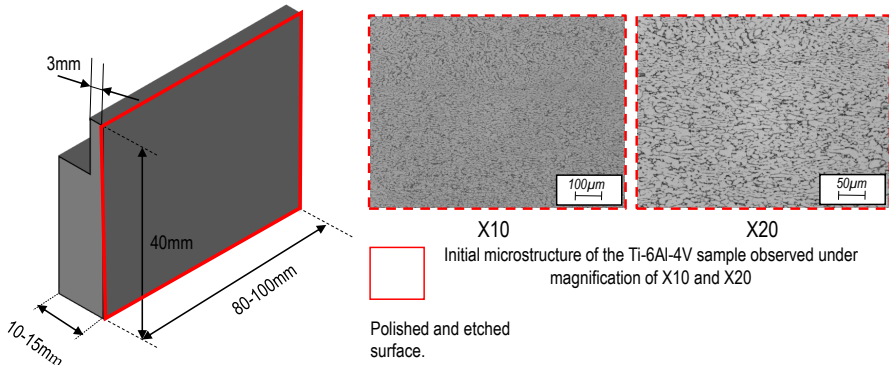


**Fig. 5** Geometry of the workpiece and Ti-6Al-4V initial microstructure.

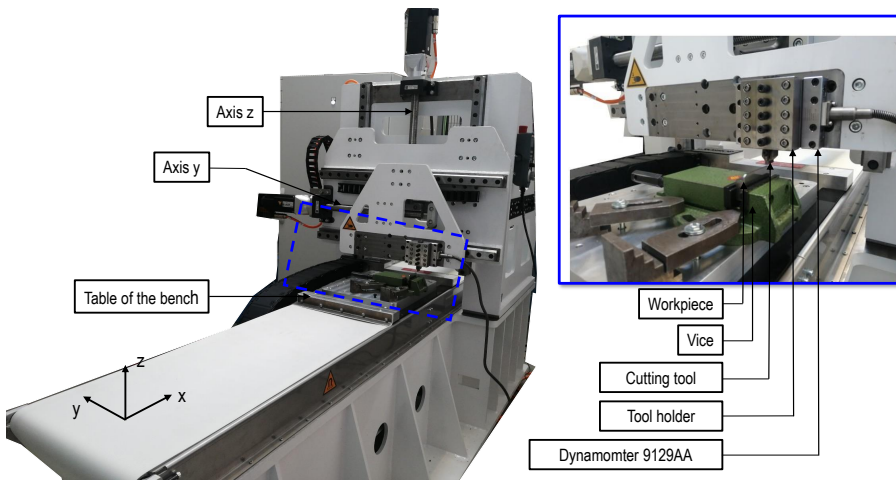


**Fig. 6** New experimental bench used for instrumented orthogonal cutting tests

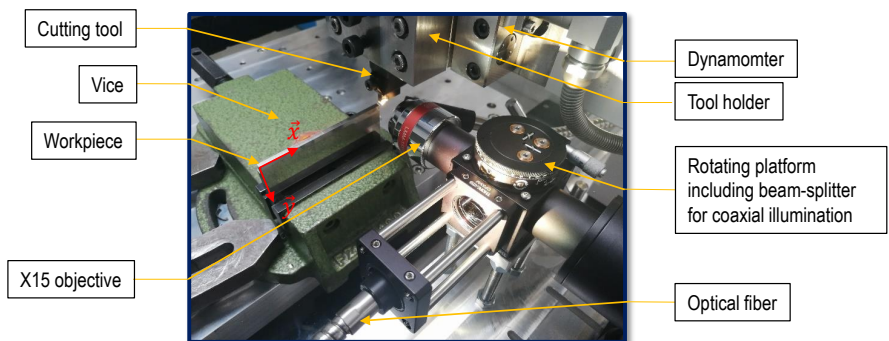


**Fig. 7** Experimental set-up for high-speed imaging of the cutting zone.

of the measured forces are summarized in Table 1. Under the same cutting speed,  $F_c$  and  $F_f$  decreases when the tool rake angle increases.

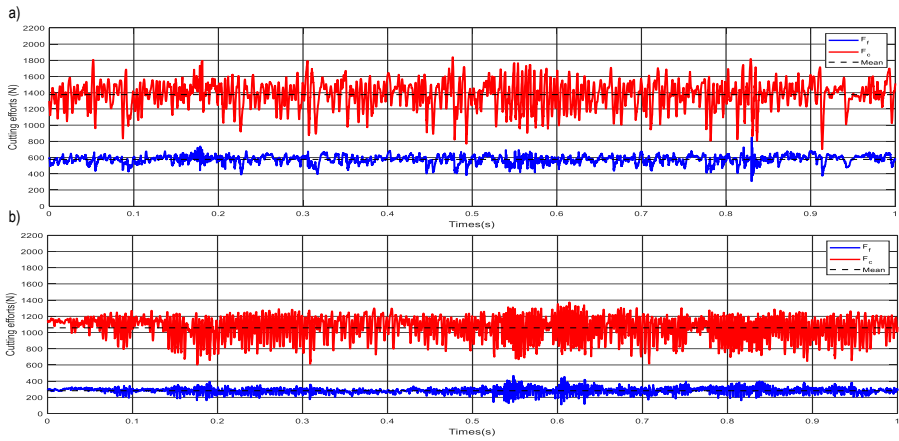


**Fig. 8** The measured cutting efforts under  $V_c=3\text{m/min}$  and: a)  $\gamma=0^\circ$  and b)  $\gamma=15^\circ$ .

**Table 1** Mean, maximum and minimum values of the measured cutting efforts.

Test n°	$F_{f,mean}$ (N)	$F_{c,mean}$ (N)
Test 1 ( $V_c=3\text{m/min}$ ; $\gamma=0^\circ$ )	577 (max:851/ min: 306) Std <sup>1</sup> (N): $\pm 51$	1377 (max:1841/ min: 701) Std (N): $\pm 166$
Test 2 ( $V_c=3\text{m/min}$ ; $\gamma=15^\circ$ )	282 (max: 469/ min: 110) Std (N): $\pm 31$	1058 (max: 1375/ min: 591) Std (N): $\pm 141$

<sup>1</sup>Std: the standard deviation of the mean value of the cutting component.

## 5 Results and discussion

### 5.1 Kinematic fields measurement

#### • Optical parameters

The camera resolution of the Fastcam APX-RS high-speed camera was set to 512x512pixels. This yields to obtain a scene size of 0,58x0,58mm<sup>2</sup> allowing for *in-situ* visualization of the material flow during Ti-6Al-4V segment chip formation. The pixel size is theoretically equal to 1,13 $\mu\text{m}$ /pixel. It was adopted for the displacement field conversion from pixel to micron unit.

The integration time was chosen so that it reduces the blur induced by the scene displacement. Setting a maximum of 2,21pixels displacement, the corresponding integration time is equal to 50 $\mu\text{s}$ .

Assuming that the speed of chip motion is equal to the cutting speed and

the segment width is equal to the feed [23], the number of images per one segment chip ( $n$ ) function of frame rate ( $f_{aq}$ ) can be predicted. Using 10000fps with a cutting speed of 3m/min and a feed of 0,2mm, theoretically 40 images per one segment chip can be obtained (equation 8 for calculation).

$$n = \frac{f_{aq} \times a}{V_c} \quad (8)$$

- **DIC parameters**

Digital Images Correlation was applied on the recorded images from the cutting zone during chip formation. Ncorr DIC software using a local approach was used [31]. The Region of Interest (ROI) was discretized into circular subset with a radius of 25pixels. The subset spacing as defined with the DIC software was set to 1pixel. This means that the distance separating two consecutive nodes is equal to 2pixels (1+subset spacing). For the strain calculation, a window with a radius of 5pixels was adopted.

- **Results of kinematic fields measurement**

Digital Image Correlation was applied on 34 images (respectively on 33 images) for the test made with  $V_c=3\text{m/min}$  and  $\gamma=0^\circ$  (respectively for the test made with  $V_c=3\text{m/min}$  and  $\gamma=15^\circ$ ). Images were chosen before the segment chip starts to slide with respect to the shear plane in order to avoid error on the computed strain fields induced by the crack propagation within the localized shear band. During Ti-6Al-4V chip segmentation, the shear strain cumulates at the tool tip and then propagates within the ASB [23, 25, 26]. Reaching the material failure, the crack starts to propagate from the tool tip towards the free surface of the workpiece. At this stage, the segment chip slides with respect to the shear plane under the assumption of rigid body motion.

Results of the measured displacement fields are given in Figure 9 and 10. The measured strain fields are given in figure 11 and 12. The displacement fields along x-axis (Figure 9.b and 10.b) and y-axis (Figure 9.c and 10.c) were obtained after conversion from pixel to micron unit.

- **Analysis**

Figure 9.a and 10.a give the visual images during Ti-6Al-4V segment chip formation as captured with the high-speed camera. It also gives the direction of the localized shear band. The cumulative displacement field along x-axis ( $U_x$ ) highlights a maximum gradient that reaches  $\approx 150\mu\text{m}$  during the final stage of segment chip formation using  $0^\circ$  rake angle while it reaches  $\approx 130\mu\text{m}$  in the case using  $15^\circ$ . The gradient of the cumulative displacement field along y-axis ( $U_y$ ) is found also higher in the case using  $0^\circ$  rake angle than in the case using  $15^\circ$ . Therefore, segment chip is more subjected to deformation in the case using  $0^\circ$  rake angle.

The measured strain fields highlight the appearance of localized shear band that is consistent with the mechanisms of Ti-6Al-4V chip formation.

At the subsurface of the workpiece and far from the machined surface,

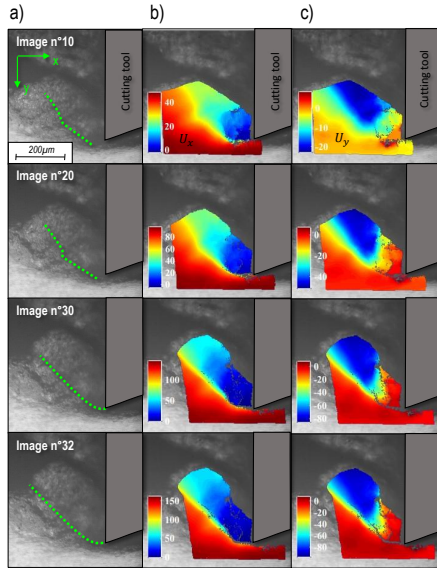


**Fig. 9** a) visual images obtained during Ti-6Al-4V segment chip formation under  $V_c=3\text{m/min}$  and  $\gamma=0^\circ$ ; b) displacement field along x-axis ( $U_x$ ) and c) displacement field along y-axis ( $U_y$ ).

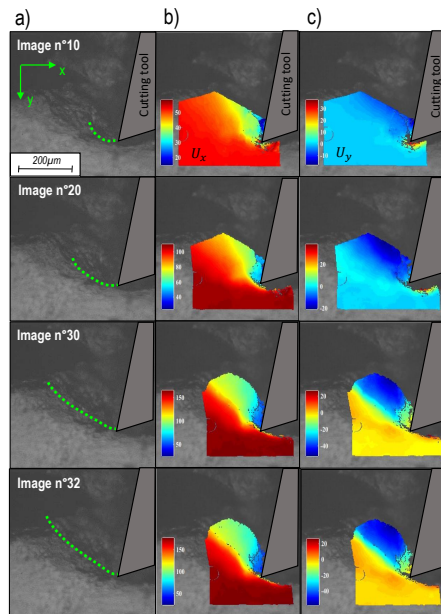


**Fig. 10** a) visual images obtained during Ti-6Al-4V segment chip formation under  $V_c=3\text{m/min}$  and  $\gamma=15^\circ$ ; b) displacement field along x-axis ( $U_x$ ) and c) displacement field along y-axis ( $U_y$ ).

the strain components were found equal to 0 which is consistent with the assumption of rigid body motion at this zone [23]. With a cutting tool of  $0^\circ$  rake angle, the equivalent strain reaches  $\approx 4$  in the localized shear band while it reaches  $\approx 3$  with a cutting tool of  $15^\circ$  rake angle. The level of the equivalent strain was found higher than the ones measured by Harzallah et al [25] under the same cutting speed ( $V_c=3\text{m/min}$ ). Initially, the experimental bench used by Harzallah et al was designed by Blanchet et al [32] to conduct instrumented orthogonal cutting tests on Carbon Fiber Reinforced Polymer (CFRP). In this work, the new experimental bench (figure 6) was designed to ensure high rigidity over hard-to-cut materials such as titanium and inconel alloys and more precision in kinematic fields measurement during orthogonal cutting.

Using  $0^\circ$  rake angle, the segment chip was found to be more subjected to compression and shear than in the case using a  $15^\circ$  rake angle. The last can be correlated with the measured cutting efforts (Table 1) where the cutting and the feed forces using  $0^\circ$  rake angle are higher than in the case using  $15^\circ$  rake angle.

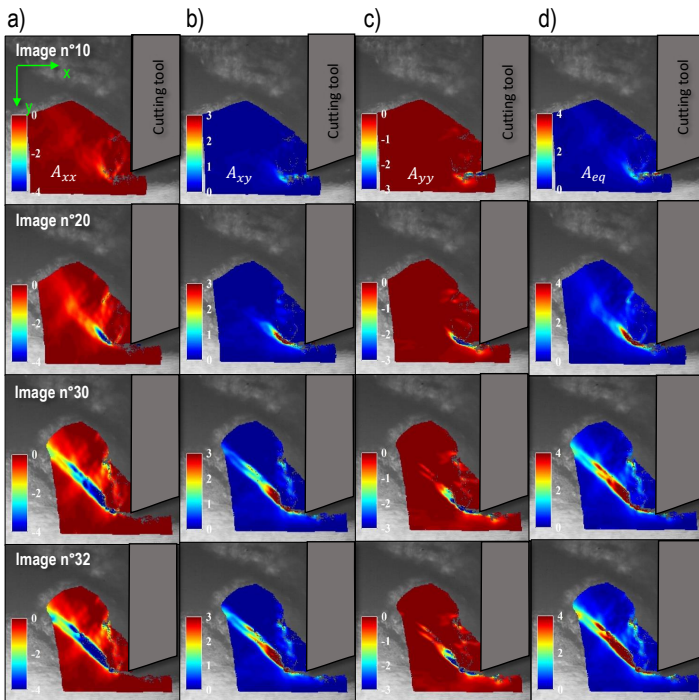


**Fig. 11** The measured Eulerian-Almansi strain components during Ti-6Al-4V chip segmentation under  $V_c=3\text{m/min}$  and  $\gamma=0^\circ$ : a)  $A_{xx}$ ; b)  $A_{xy}$ ; c)  $A_{yy}$  and d)  $A_{eq}$ .

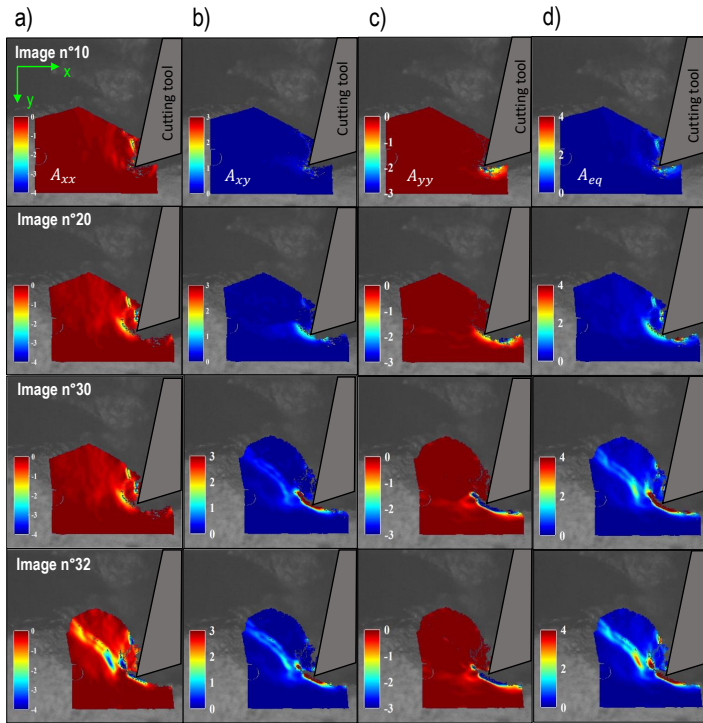


**Fig. 12** The measured Eulerian-Almansi strain components during Ti-6Al-4V chip segmentation under  $V_c=3\text{m/min}$  and  $\gamma=15^\circ$ : a)  $A_{xx}$ ; b)  $A_{xy}$ ; c)  $A_{yy}$  and d)  $A_{eq}$ .

- **Accuracy assessment**

The main source of errors in strain field measurement within the cutting zone is the out-of-plane motion of the chip. In order to evaluate the accuracy of the measured strain fields, the effect of out-of-plane displacement was examined. An out-of-plane displacement with an increment of  $10\mu\text{m}$  was applied along the optical axis and an image was recorded at each step. The mean value of the virtual equivalent strain was measured.

The result of the measured mean value of the virtual equivalent strain function of the out-of-plane displacement and for different subset radius is given in figure 13. Using a subset radius of 25pixels, the maximum mean value of the virtual equivalent strain reaches  $\approx 6,5 \cdot 10^{-2}$  which is negligible comparing to the measured equivalent strain reached in the localized shear band ( $\approx 4$  using  $0^\circ$  rake angle and  $\approx 3$  using  $15^\circ$  rake angle). The last proves the property of the DIC application for kinematic fields measurement during orthogonal cutting and therefore reliability of the measured strain fields.

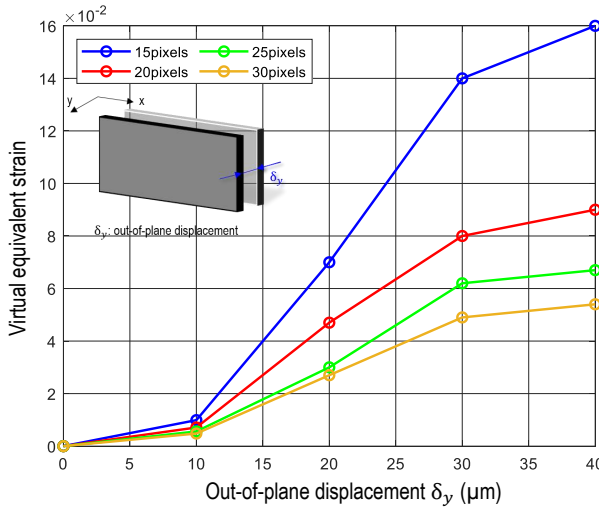


**Fig. 13** Mean value of the virtual equivalent strain function of the out-of-plane displacement and for different subset radius.

## 6 Chip morphology and characteristic

### • Chip morphology analysis

A Scanning Electron Microscopy (SEM) view was made on Ti-6Al-4V chip. Segmented chips were observed highlighting crack opening within the localized shear band and high material failure near the tool-chip contact zone (figure 14). The last gives one of the main difficulties of the DIC application in the context of kinematic fields measurement during orthogonal cutting. Material discontinuity induced by crack implies subset truncation for more accuracy in the measured strain fields.

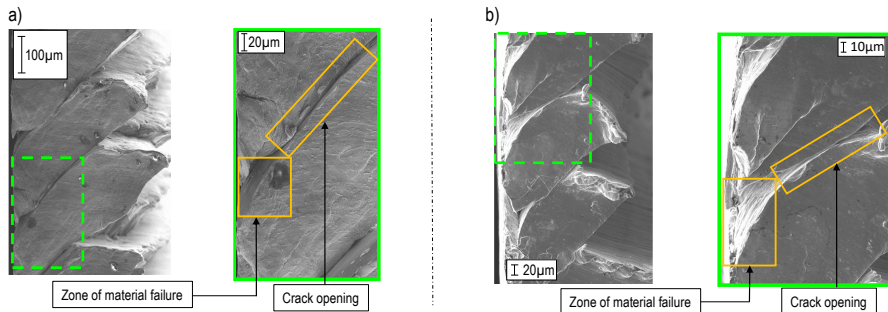


**Fig. 14** SEM view on Ti-6Al-4V chip obtained during orthogonal cutting under  $V_c=3\text{m}/\text{min}$  and: a)  $\gamma=0^\circ$  and b)  $\gamma=15^\circ$ .

- **Chip microstructure analysis**

Collected chips were polished and etched in order to study the impact of the cutting process on the material microstructure. SEM views (figure 15) were made on the Ti-6Al-4V chips. A focus was done on the primary and the secondary shear zones. A deformed  $\beta$ -phase was observed within the adiabatic shear band. Elongated  $\beta$ -phase was observed within the SSZ. The width of the SSZ in the case using  $0^\circ$  rake angle (figure 15.a) is equal to  $18,5\mu\text{m}$ . Less elongated  $\beta$ -phase was observed in the SSZ when using a  $15^\circ$  rake angle (figure 15.b). The last proves that material within the SSZ is more subjected to deformation in the case using  $0^\circ$  rake angle.

Figure 15 shows crack near the free surface of the chip which is not connected to the tool-chip contact zone. Indeed, this observation is made through the width of the chip after material removal due to polishing. It highlights the difference between crack formation at the surface of the chip (figure 14) and through the width (figure 15). As mentioned by Komanduri et al [33] and proven by Pottier et al [23] (after observation of the chip through thickness), this results from the high hydrostatic stress zone within the center of the chip which disables crack formation near the tool-chip contact zone.

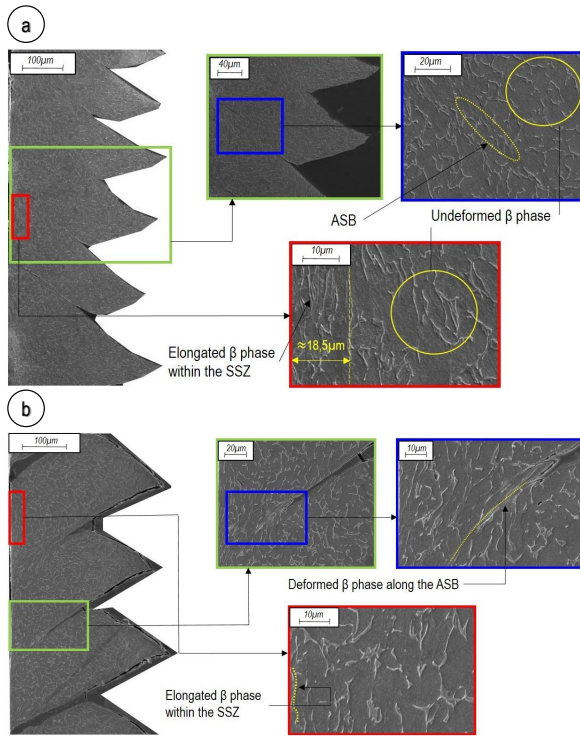


**Fig. 15** Ti-6Al-4V chip microstructure obtained after orthogonal cutting under  $V_c=3\text{m}/\text{min}$  and: a)  $\gamma=0^\circ$  and b)  $\gamma=15^\circ$ .

- **Segment width analysis**

The recorded video of the cutting process was obtained with sufficient quality allowing for chip characteristics to be measured for different segments (Figure 16). Only the segment width was measured in order to study the effect of the rake angle on the chip compression.

Occurrence of the chip segment width was fitted with a normal distribution in order to determine the mean value of the chip segment width for both the tests. In the case using a  $0^\circ$  rake angle (figure 16.a), the mean value of the chip segment width is equal to 0,17mm which is slightly lower than in the case using  $15^\circ$  rake angle (figure 16.b) as the mean value of the chip segment width was found equal to 0,19mm.

The last can be traced back to the fact that the chip segment is more subjected to compression along x- and y-axis ( $A_{xx}$  and  $A_{yy}$ ) in the case using  $0^\circ$  rake angle (Figure 11.a and c) than in the case using  $15^\circ$  rake angle (Figure 12.a and c).

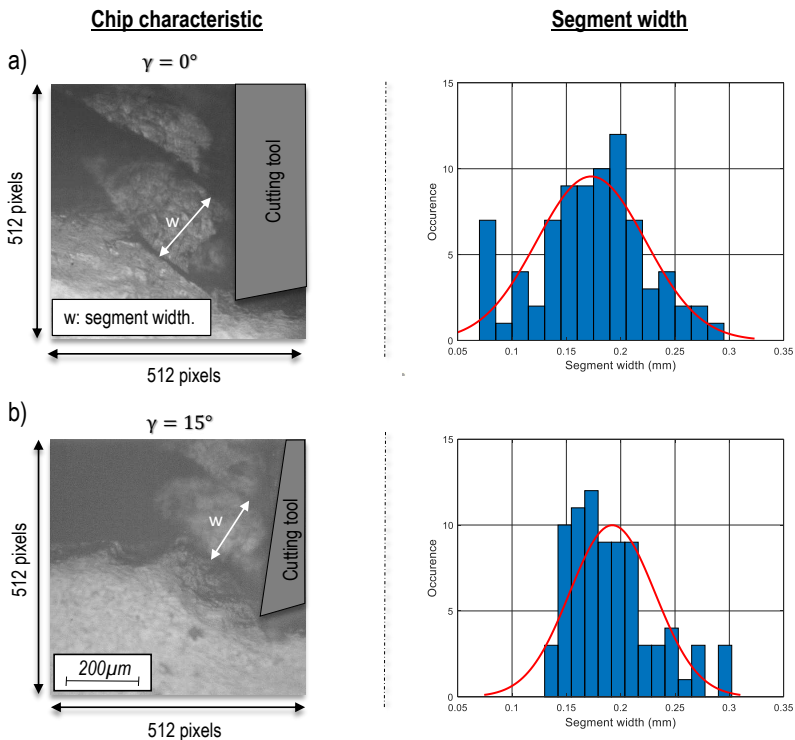


**Fig. 16** Ti-6Al-4V chip characteristic and occurrence of chip segment width measured from the recorded video obtained during orthogonal cutting under  $V_c=3\text{m/min}$  and: a)  $\gamma=0^\circ$  and b)  $\gamma=15^\circ$ .

## 7 Conclusion

This paper outlines the methodology and technique used for kinematic fields measurement during orthogonal cutting and thus a local scale analysis of Ti-6Al-4V chip formation. In-situ visualization of the material flow during chip formation remains a non-trivial task regarding the submillimetric size of the cutting zone and the rapidity of the orthogonal cutting process.

A dedicated optical system using beam-splitter for coaxial illumination that made possible to reveal the material microstructure considered as a natural speckle for particle tracking was proposed. Application of the DIC technique on the recorded images yields to measure the kinematic fields.

The measured strain fields highlight the appearance of localized shear band which is consistent with the mechanisms of Ti-6Al-4V chip formation. Indeed, the segment chip was found to be subjected mainly to shear and compression. Moreover, at the subsurface of the workpiece and far from the machined surface, the measured strain fields was found equal to 0 which match with the assumption of rigid body motion at this zone.

In order to evaluate the property of the DIC application, the effect of out-of-plane displacement was examined. The mean value of the virtual equivalent strain was found negligible compared to the measured equivalent strain reached in the localized shear band and thus proves the reliability of the measured strain fields.

Correlation between the measured strain fields along x- and y-axis and the mean value of the chip segment width was made in order to reveal the effect of the cutting tool rake angle. Indeed, using a 0° rake angle, the chip segment was found to be more subjected to compression which explains the fact that the mean value of the chip segment width is lower compared to the case using 15° rake angle.

In future work, instrumented orthogonal cutting tests on Ti-6Al-4V will be conducted with higher cutting speeds. This require increasing the frame rate and the light intensity that leads to reduce the integration time in order to obtain good images qualities under cutting speeds that may be closer from the used ones in industry.

**Supplementary information.** no supplementary information

**Acknowledgments.** This project received funding from the European Union's Marie Skłodowska-Curie Actions (MSCA) Innovative Training Networks (ITN) H2020-MSCA-ITN-2017 under the grant agreement N°764979.

## Declarations

Not applicable

- Funding
- Conflict of interest/Competing interests (check journal-specific guidelines for which heading to use)

- Ethics approval
- Consent to participate
- Consent for publication
- Availability of data and materials
- Code availability
- Authors' contributions

Editorial Policies for:

Springer journals and proceedings:

<https://www.springer.com/gp/editorial-policies>

Nature Portfolio journals:

<https://www.nature.com/nature-research/editorial-policies>

*Scientific Reports*:

<https://www.nature.com/srep/journal-policies/editorial-policies>

BMC journals:

<https://www.biomedcentral.com/getpublished/editorial-policies>

## References

- [1] V. Wagner, F. Barelli, G. Dessen, R. Laheurte, P. Darnis, O. Cahuc, M. Mousseigne, Comparison of the chip formations during turning of Ti64  $\beta$  and Ti64  $\alpha+\beta$ , *Journal of Engineering Manufacture*, 233 (2017) pp.0954405417728309.
- [2] V. Wagner, F. Barelli, G. Dessen, R. Laheurte, P. Darnis, O. Cahuc, M. Mousseigne, Thermal and microstructure study of the chip formation during turning of a lamellar titanium structure : the Ti64  $\beta$ , *Journal of Manufacturing Science and Engineering*, 140 (2017) pp.031010.
- [3] X.P Zhang, R. Shivpuri, A.K. Srivastava, Role of phase transformation in chip segmentation during high speed machining of dual phase titanium alloys, *Journal of Materials Processing Technology*, 214 (2014) 3048-3066.
- [4] S.N. Melkote, R. Liu, P. Fernandez-Zelaia, T. Marusich, A physically based constitutive model for simulation of segmented chip formation in orthogonal cutting of commercially pure titanium, *CIRP Annals - Manufacturing Technology*, 64 (2015) 65-68.
- [5] A. Li, J. Pang, J. Zhao, J. Zang, F. Wang, FEM-simulation of machining induced surface plastic deformation and microstructural texture evolution of Ti-6Al-4V alloy, *International Journal of Mechanical Sciences*, 123 (2017) 214-223.

- [6] Y. Huang, J. Ji, K.M. Lee, An improved material constitutive model considering temperature-dependent dynamic recrystallization for numerical analysis of Ti-6Al-4V alloy machining, *International Journal of Advanced Manufacturing Technology*, 97 (2018) 3655-3670.
- [7] T. Baizeau, S. Campocasso, G. Fromentin, R. Besnard, Kinematic field measurements during orthogonal cutting tests via DIC with double-frame camera and pulsed laser lighting, *Experimental Mechanics*, 57 (2017) 581-591.
- [8] Z. H. Yang, X. M. Zhang, G. C. Nie, D. Zhang, H. Ding, A comprehensive experiment-based approach to generate stress field and slip lines in cutting process, *Journal of Manufacturing Science and Engineering*, 143 (2021) pp. 071014.
- [9] B. Thimm, J. Steden, M. Reuber, H. J. Christ, Using Digital Image Correlation Measurements for the Inverse Identification of Constitutive Material Parameters applied in Metal Cutting Simulations. In: E. Ozturk, ed. 17th CIRP Conference on Modelling of Machining Operations, Sheffield, 13-14 June 2019. United Kingdom, pp95-100.
- [10] M. Calamaz, D. Coupard, F. Girot, Numerical simulation of titanium alloy dry machining with a strain softening constitutive law, *Machining Science and Technology*, 14 (2010) 244-257
- [11] G. Rotella, O. Dillon, D. Umbrello, L. Settineri, I. Jawahir, Finite element modeling of microstructural changes in turning of AA7075-t651 alloy, *Journal of Manufacturing Processes*, 15 (2013) 87-95
- [12] F. Jafarian, M.I. Ciaran, D. Umbrello, P.J. Arrazola, L. Filice, H. Amirabadi, Finite element simulation of machining Inconel 718 alloy including microstructure changes, *International Journal of Mechanical Sciences*, 88 (2014) 110-121
- [13] Q. Wang, Z. Liu, B. Wang, Q. Song, Y. Wan, Evolutions of grain size and micro-hardness during chip formation and machined surface generation for Ti-6Al-4V in high-speed machining, *International Journal of Advanced Manufacturing Technology*, 82 (2016) 1725-1736
- [14] J.L Battaglia, L. Puigsegur, O. Cahuc, Estimated temperature on a machined surface using an inverse approach, *Experimental Heat Transfer*, 18 (2006) 13-32
- [15] O. Cahuc, P. Darnis, R. Laheurte, Mechanical and thermal experiments in cutting process for new behaviour law, *International Journal of Forming Processes*, 10 (2007) 235-269

- [16] S. Atlati, B. Haddag, M. Nouari, M. Zenasni, Thermomechanical modelling of the tool–workmaterial interface in machining and its implementation using the ABAQUS VUINTER subroutine, *International Journal of Mechanical Sciences*, 87 (2014) 102-117
- [17] B. Haddag, S. Atlati, M. Nouari, M. Zenasni, Analysis of the heat transfer at the tool–workpiece interface in machining: determination of heat generation and heat transfer coefficients, *Heat Mass Transfer*, 51 (2015) 1355-1370
- [18] A. Hijazi, V. Madhavan, A novel ultra-high speed camera for digital image processing applications, *Measurement Science and Technology*, 19 (2008) pp.085503
- [19] J. Pujana, P.J. Arrazola, J.A Villar, In-process high-speed photography applied to orthogonal turning, *Journal of materials processing technology*, 202 (2008) 475-485
- [20] H. Ghadbeigi, S.R. Bradbury, C. Pinna, J.R. Yates, Determination of micro-scale plastic strain caused by orthogonal cutting, *International Journal of Machine Tools and Manufacture*, 45 (2008) 228-235
- [21] K. Bitans, R. H. Brown, TAn investigation of the deformation in orthogonal cutting, *International Journal of Machine Tool Design and Research*, 5 (1965) 155-165.
- [22] T. Vorm, Development of a quick-stop device and an analysis of the "frozen-chip" technique, *International Journal of Machine Tool Design and Research*, 16 (1976) 241-250.
- [23] T. Pottier, G. Germain, M. Calamaz, A. Morel, D. Coupard, Sub-Millimeter Measurement of Finite Strains at Cutting Tool Tip Vicinity, *Expeimental Mechanics*, 54 (2014) 1031-1042.
- [24] D. Zhang, X. M. Zhang, W. J. Xu, H. Ding, Stress Field Analysis in Orthogonal Cutting Process Using Digital Image Correlation Technique, *Journal of Manufacturing Science and Engineering*, 139 (2017) pp. 03100.
- [25] M. Harzallah, T. Pottier, R. Gilblas, Y. Landon, M. Mousseigne, J. Senatore, A coupled in-situ measurement of temperature and kinematic fields in Ti-6Al-4V serrated chip formation at micro-scale, *International Journal of Machine Tools and Manufacture*, 130-131 (2018) 20-35.
- [26] B. Davies, D. Dabrow, P. Ifju, G. Xiao, S. Y. Liang, Y. Huang, Study of the Shear Strain and Shear Strain Rate Progression during Titanium Machining , *Journal of Manufacturing Science and Engineering*, 140 (2018) pp. 051007.

- [27] M. Meurer, T. Augspurger, B. Tekkaya, D. Schraknepper, A. P. Lima, T. Bergs, Development of a methodology for strain field analysis during orthogonal cutting. In: P.J. Arrazola, ed. 5th CIRP Conference on Surface Integrity. Online, 1-5 June 2020. pp.444-449.
- [28] H. Zouabi, M. Calamaz, V. Wagner, O. Cahuc, G. Dessein, Kinematic fields measurement during orthogonal cutting using digital images correlation: a review, *Journal of Manufacturing and Materials Processing*, 5 (2021) 1-23.
- [29] M. Calamaz, D. Coupard, F. Girot, Strain Field Measurement in Orthogonal Machining of a Titanium Alloy, *Journal of Advanced Materials Research*, 498 (2012) 237-242.
- [30] B. Pan, K. Qian, H. Xie, A. Asundi, Two-dimensional digital image correlation for in-plane displacement and strain measurement: a review, *Measurement Science and Technology*, 20 (2009) pp. 062001.
- [31] J. Blaber, B. Adair, A. Antoniou, Ncorr: open-source 2D digital image correlation matlab software, *Experimental Mechanics*, 55 (2015) 1105-1122.
- [32] F. Blanchet, Etude de la coupe par le biais d'essais élémentaires en coupe orthogonale. Application aux composites Carbone/Epoxy, Thèse de doctorat, Université de Toulouse (2015).
- [33] R. Komanduri, B.F. Von Turkovich, New observations on the mechanisms of chip formation when machining titanium alloys, *Journal of Wear*, 69 (1981) 179-188.